Earth and Planetary Science Letters 481 (2018) 125–135

Contents lists available at ScienceDirect

Earth and Planetary Science Letters

www.elsevier.com/locate/epsl

Evidence for local and global redox conditions at an Early Ordovician (Tremadocian) mass extinction

Cole T. Edwards [a,b,*], David A. Fike [b], Matthew R. Saltzman [c], Wanyi Lu [d], Zunli Lu [d,**]

[a] Department of Geological and Environmental Sciences, Appalachian State University, Boone, NC 28608, USA
[b] Department of Earth and Planetary Sciences, Washington University, St. Louis, MO 63130, USA
[c] School of Earth Sciences, The Ohio State University, Columbus, OH 43214, USA
[d] Department of Earth Sciences, Syracuse University, Syracuse, NY 13244, USA

ARTICLE INFO

Article history:
Received 29 May 2017
Received in revised form 20 September 2017
Accepted 1 October 2017
Available online xxxx
Editor: D. Vance

Keywords:
Ordovician
anoxia
carbon isotopes
sulfur isotopes
I/Ca
extinction

ABSTRACT

Profound changes in environmental conditions, particularly atmospheric oxygen levels, are thought to be important drivers of several major biotic events (e.g. mass extinctions and diversifications). The early Paleozoic represents a key interval in the oxygenation of the ocean–atmosphere system and evolution of the biosphere. Global proxies (e.g. carbon ($\delta^{13}C$) and sulfur ($\delta^{34}S$) isotopes) are used to diagnose potential changes in oxygenation and infer causes of environmental change and biotic turnover. The Cambrian–Ordovician contains several trilobite extinctions (some are apparently local, but others are globally correlative) that are attributed to anoxia based on coeval positive $\delta^{13}C$ and $\delta^{34}S$ excursions. These extinction and excursion events have yet to be coupled with more recently developed proxies thought to be more reflective of local redox conditions in the water column (e.g. I/Ca) to confirm whether these extinctions were associated with oxygen crises over a regional or global scale.

Here we examine an Early Ordovician (Tremadocian Stage) extinction event previously interpreted to reflect a continuation of recurrent early Paleozoic anoxic events that expanded into nearshore environments. $\delta^{13}C$, $\delta^{34}S$, and I/Ca trends were measured from three sections in the Great Basin region to test whether I/Ca trends support the notion that anoxia was locally present in the water column along the Laurentian margin. Evidence for anoxia is based on coincident, but not always synchronous, positive $\delta^{13}C$ and $\delta^{34}S$ excursions (mainly from carbonate-associated sulfate and less so from pyrite data), a 30% extinction of standing generic diversity, and near-zero I/Ca values. Although evidence for local water column anoxia from the I/Ca proxy broadly agrees with intervals of global anoxia inferred from $\delta^{13}C$ and $\delta^{34}S$ trends, a more complex picture is evident where spatially and temporally variable local trends are superimposed on time-averaged global trends. Stratigraphic sections from the distal and deeper part of the basin (Shingle Pass and Meiklejohn Peak) preserve synchronous global ($\delta^{13}C$ and $\delta^{34}S$) and water column (I/Ca) evidence for anoxia, but not at the more proximal section (Ibex, UT). Although geochemical and paleontological evidence point toward anoxia as the driver of this Early Ordovician extinction event, differences between I/Ca and $\delta^{13}C$–$\delta^{34}S$ signals suggest regional variation in the timing, extent, and persistence of anoxia.

© 2017 Elsevier B.V. All rights reserved.

1. Introduction

Changing environmental conditions, including climatic warming and cooling (McInerney and Wing, 2011; Trotter et al., 2008) and (de-)oxygenation of the ocean–atmosphere system (Berner et al., 2007; Fike et al., 2006), are thought to be important drivers of several major biotic events of the Phanerozoic. Few direct and well-calibrated geochemical proxies are available to characterize these phenomena in the rock record, so instead one must rely on combining multiple independent proxies that collectively constrain the magnitude, timing, and causes of environmental change. For example, evidence for changes in atmospheric oxygen is traditionally based on isotope mass balance and paired stable carbon ($\delta^{13}C$) and sulfur ($\delta^{34}S$) isotope excursions (Adams et al., 2010; Berner, 2006; Gill et al., 2011, 2007; Gomes et al., 2016; Jones and Fike, 2013; Kah et al., 2016; Owens et al., 2013). These well-established isotope systems are thought to signify changing global redox conditions (e.g. bottom-water anoxia, or euxinia if sulfide

* Corresponding author at: Department of Geological and Environmental Sciences, Appalachian State University, Boone, NC 28608, USA.
** Corresponding author.
E-mail addresses: edwardsct4@appstate.edu (C.T. Edwards), zunlilu@syr.edu (Z. Lu).

https://doi.org/10.1016/j.epsl.2017.10.002
0012-821X/© 2017 Elsevier B.V. All rights reserved.

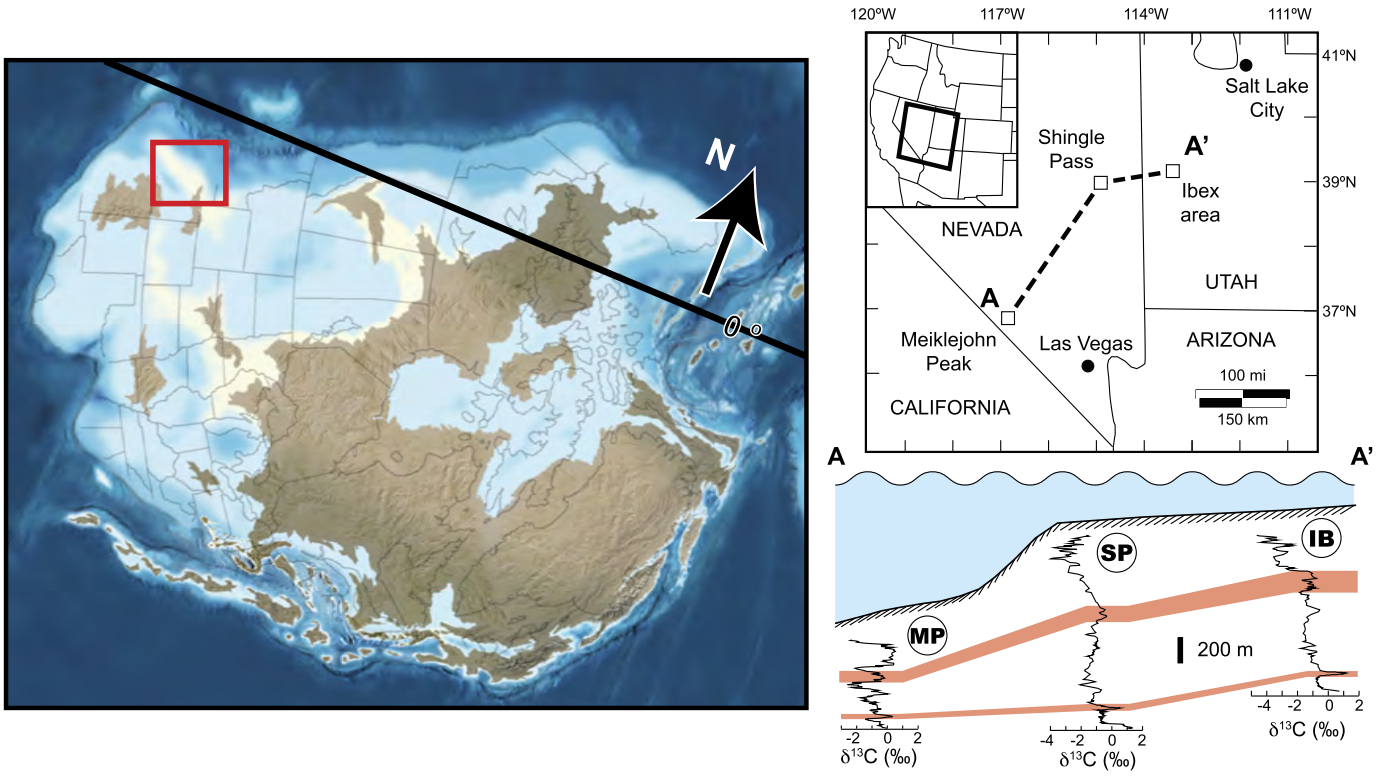

Fig. 1. *Left*: Paleogeographic reconstruction of Laurentia during the Middle Ordovician (470 Myr ago) and the approximate location of the equator. Modified from Blakey (2011). *Right*: Map of Great Basin region, western United States (red box from *left*), and location of the three studied sections with a diagrammatic overview of proximal-to-distal transect (A–A′) along the shelf with $\delta^{13}C$ trends (Edwards and Saltzman, 2016) from the Ibex area (IB), Shingle Pass (SP), and Meiklejohn Peak (MP). Conodont-calibrated positive excursions correlated in red, showing thickness variations between sections and a more condensed interval in the distal, deeper Meiklejohn Peak section. Lowermost excursion represents the Skullrockian–Stairsian excursion studied herein. (For interpretation of the references to color in this figure legend, the reader is referred to the web version of this article.)

is present in the water column) that influence organic matter and pyrite burial rates. Modeling of $\delta^{34}S$ excursions can provide reasonable estimates of anoxia or euxinia (Gill et al., 2011, 2007; Gomes et al., 2016; Owens et al., 2013), but these conclusions are based on assumptions about the size and homogeneity of the global sulfate reservoir and its fluxes (*i.e.* pyrite burial rates), thus giving only indirect proxy evidence for oxygenation. More recently, newly developed geochemical proxies such as trace element abundances are thought to more directly record redox conditions of local to regional waters at the site of mineral precipitation, either from porewater or overlying water column. Specific applications include Fe-speciation (Li et al., 2010), U, Mo, Cr and other trace metal isotopes and concentrations (Gill et al., 2011; Jin et al., 2016; Owens et al., 2017, 2016; Reinhard et al., 2013), and I/Ca (Lu et al., 2010; Zhou et al., 2015). Whereas all of these individual proxies may be differentially susceptible to potential alteration, their combined use can shed new light on local environmental conditions. When trace element proxies are combined with more well-established methods for estimating de-oxygenation based on global reservoirs (e.g. carbon and sulfur), particularly when paired with paleontological data that record diversification or extinction of faunas locally, this can provide new insight about oxygen levels during key intervals of Earth history and allow for improved calibration of indirect and direct redox proxies.

The Cambrian–Ordovician represents a key interval in the evolution of the biosphere where several globally recognized extinctions of trilobite groups (i.e. "biomeres") occurred (e.g. Saltzman et al., 2015). The causes of these extinctions are attributed to episodic upwelling of anoxic waters into shallow shelf environments during sea-level rise, an interpretation based on coeval positive $\delta^{13}C$ and $\delta^{34}S$ excursions inferred to reflect elevated organic and pyrite burial rates, respectively, under anoxic or euxinic conditions (Gill et al., 2011; Saltzman et al., 2015). If excursions of anoxic waters into shelf environments were the dominant driver of Cambrian–Ordovician trilobite extinctions, then both local and global proxies for anoxia are expected to provide complementary evidence as the cause of ecological turnover of marine communities and elevated extinction rates.

In this study we sampled three Lower Ordovician (Tremadocian Stage) carbonate successions in the Great Basin region (Fig. 1) where one of youngest extinction events (i.e. biomere boundaries) and $\delta^{13}C$ excursions is well documented (Saltzman et al., 2015). The parallel $\delta^{13}C$ and $\delta^{34}S$ excursions in this Lower Ordovician succession can be used as a test case to evaluate the I/Ca proxy for its potential to faithfully record marine anoxia, previously interpreted as the cause of a local trilobite extinction (Saltzman et al., 2015). Building upon published $\delta^{13}C$ curves ($\delta^{13}C_{carb}$; Edwards and Saltzman, 2016), we combine new $\delta^{34}S$ data from carbonate-associated sulfate (CAS; $\delta^{34}S_{CAS}$) and pyrite ($\delta^{34}S_{py}$) with I/Ca measured from bulk carbonate (mostly lime, but rarely dolomitic) mudstone facies to investigate the degree to which local marine anoxia occurred along a proximal-to-distal transect. We combine geochemical trends with published paleontological data from the shallow-water section at Ibex to explore how diversification and extinction rates of local faunas compare to proxy evidence for de-oxygenation.

2. Background

2.1. Geologic setting and geochemical records

Lower Ordovician strata in the Great Basin region are interpreted to have accumulated on a carbonate ramp, which covered

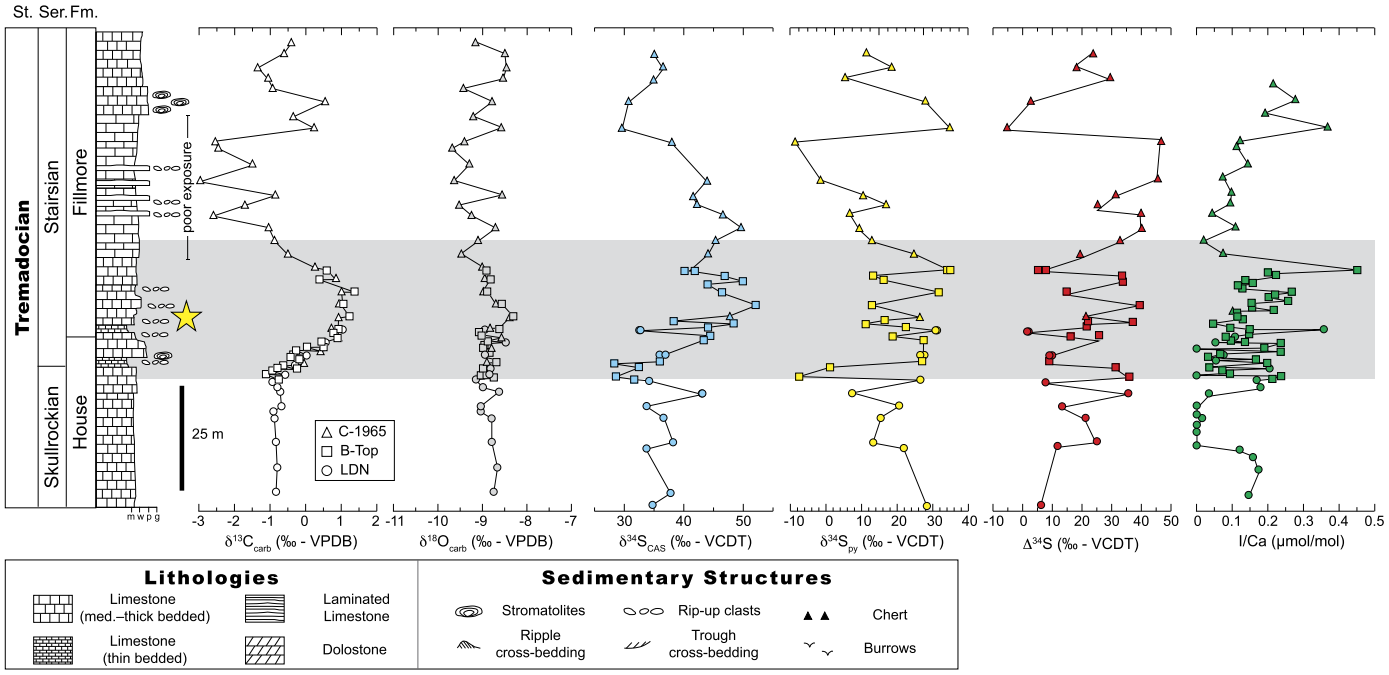

Fig. 2. Lithologic facies and geochemical trends from the Ibex area, UT. During the base-Stairsian $\delta^{13}C_{carb}$ positive excursion (gray box), $\delta^{34}S_{CAS}$, and to a lesser extent $\delta^{34}S_{py}$, also records positive excursions, but $\Delta^{34}S$ shows no overall trend throughout this interval due to sample-to-sample $\delta^{34}S$ variability. I/Ca values decrease to near zero prior to the onset of the $\delta^{13}C$ and $\delta^{34}S$ excursions (see main text for discussion). Data from Ibex comes from a composite of three sections across the House–Fillmore interval (Saltzman et al., 2015). Yellow star indicates location of CL analysis of thin section B-TOP 7416 (see Fig. 5). Age estimates are based on biostratigraphic and sequence stratigraphic data presented in Adrain et al. (2014), Miller et al. (2012), and Ethington and Clark (1981). St. = Stage, Ser. = North American Series, Fm. = Formation, m = mudstone, w = wackestone, p = packstone, g = grainstone. (For interpretation of the references to color in this figure legend, the reader is referred to the web version of this article.)

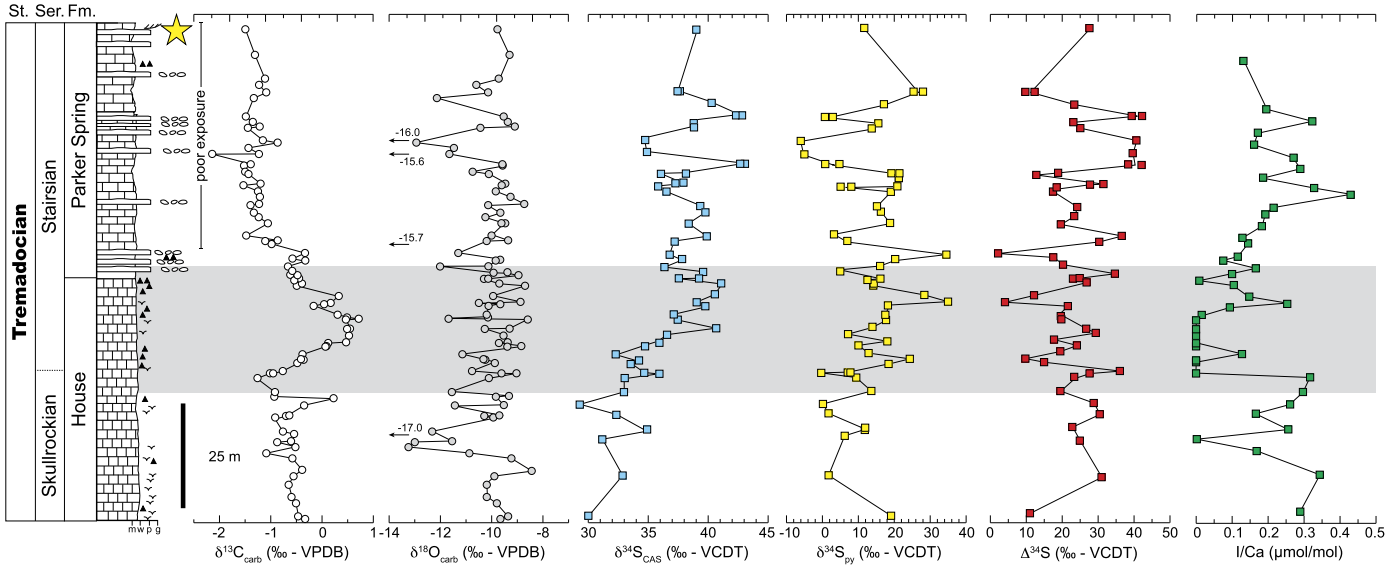

Fig. 3. Lithologic facies and geochemical trends from Shingle Pass, NV. The onset of the base-Stairsian $\delta^{13}C_{carb}$ positive excursion (gray box) co-occurs with a $\delta^{34}S_{CAS}$ excursion, but $\delta^{34}S_{CAS}$ does not return to baseline values along with $\delta^{13}C_{carb}$. $\delta^{34}S_{py}$ records a weak positive excursion coincident with $\delta^{34}S_{CAS}$. Symbols and abbreviations from Fig. 2. Yellow star indicates location of CL analysis of thin section SP 7553 (see Fig. 5). Age estimates based on conodont biostratigraphy of Sweet and Tolbert (1997). (For interpretation of the references to color in this figure legend, the reader is referred to the web version of this article.)

the Cambrian growth fault-controlled House Range embayment (e.g. Miller et al., 2012 and refs. within), and deepened away from the continental interior near the paleo-equator (Fig. 1; Ross et al., 1989). Strata studied here comprise the lower Pogonip Group and are recognized as the House Limestone and Fillmore Fm. at Ibex (Fig. 2), the House Limestone and Parker Spring Fm. at Shingle Pass (Fig. 3), and the Goodwin Fm. at Meiklejohn Peak (Fig. 4). Carbonate lithologies include fine-grained lime mud- to wackestone (with rare dolomitic intervals) interbedded with siliciclastic silt laminae and occasional thin shale beds. Occasional coarse-grained lithologies include trilobite packstone to grainstone, as well as flat pebble conglomerate (Saltzman et al., 2015). These sections have yet to be placed within a sequence stratigraphic framework, so temporal relationships between facies currently rely on geochemical trends (i.e. $\delta^{13}C_{carb}$; Edwards and Saltzman, 2016) and paleontological data (Ethington and Clark, 1981; Sweet and Tolbert, 1997). Petrographic fabrics and $\delta^{13}C$ and $\delta^{18}O$ compositions of the lower Pogonip Group strata do not show evidence of intense meteoric di-

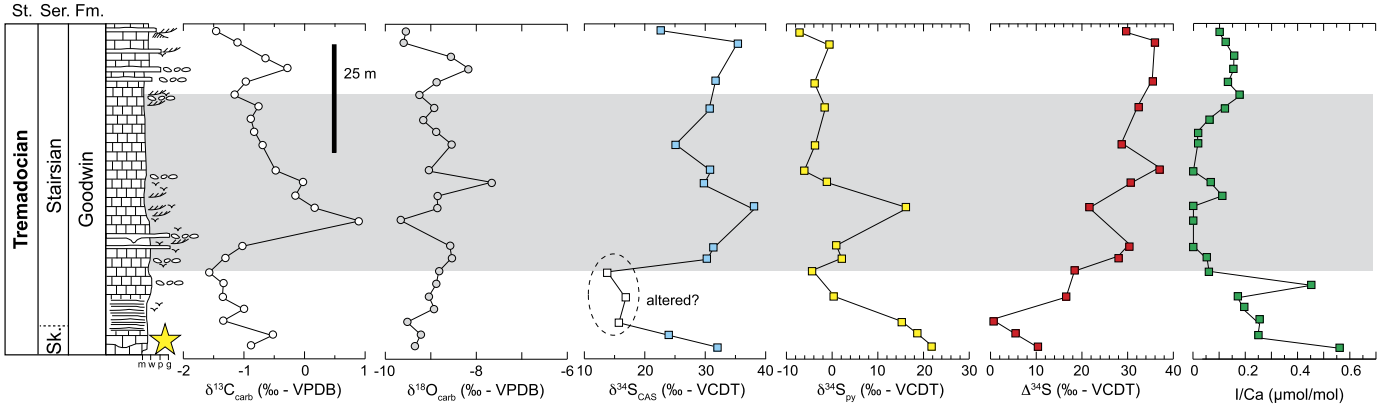

Fig. 4. Lithologic facies and geochemical trends from Meiklejohn Peak, NV. The $\delta^{13}C_{carb}$ positive excursion (gray box) is coeval with apparent $\delta^{34}S_{CAS}$ and $\delta^{34}S_{py}$ excursions, although a possible brief negative excursion that occurs prior to the positive $\delta^{13}C_{carb}$ excursion would diminish the magnitude of the $\delta^{34}S$ perturbation at Meiklejohn Peak (see main text for discussion). Symbols and abbreviations from Fig. 2. Yellow star indicates location of CL analysis of thin section MP 291 (see Fig. 5). (For interpretation of the references to color in this figure legend, the reader is referred to the web version of this article.)

agenesis (Edwards and Saltzman, 2014). A high-resolution $\delta^{13}C_{carb}$ profile across the House–Fillmore interval at Ibex, the most proximal of the three sections, shows a well-defined positive $\delta^{13}C_{carb}$ excursion within a few meters of a major extinction of both trilobites and conodonts (Saltzman et al., 2015). Saltzman et al. (2015) interpret this extinction event as the result of sea-level rise and the associated expansion of anoxic waters into shallow shelf environments. This Lower Ordovician $\delta^{13}C_{carb}$ excursion at the North American Skullrockian–Stairsian Stage boundary appears to represent a global event (Saltzman et al., 2015).

Lower Ordovician carbonates from the Great Basin region have been previously studied for $\delta^{13}C_{carb}$ trends and shown to be regionally and globally correlative (Edwards and Saltzman, 2016, 2014; Saltzman et al., 2015). In particular, a prominent 1–1.5‰ positive excursion in $\delta^{13}C_{carb}$ occurs near the base of the Low Diversity Interval conodont biozone, which has been reported from sections around the global (e.g. New Mexico (USA), Argentina, South Korea; Saltzman et al., 2015). Preliminary $\delta^{34}S_{CAS}$ data have also been reported from this interval (Shingle Pass, NV) where a ~10‰ positive $\delta^{34}S_{CAS}$ excursion is coeval with the $\delta^{13}C_{carb}$ excursion (Saltzman et al., 2015).

2.2. Global geochemical redox proxies

Parallel changes in $\delta^{13}C$ and $\delta^{34}S$ preserved in coeval stratigraphic sections around the world are often interpreted to record changes in redox conditions driven by a global cause (e.g. Berner, 2006; Gill et al., 2007). Because ocean circulation timescales (10^3 yr) are significantly shorter than the residence times of carbon (10^5 yr) and sulfate (10^6 yr) in the global ocean reservoirs, oceans are considered well mixed with respect to the carbon and sulfur isotopic composition of seawater, although a single-reservoir model may not accurately reflect the global sulfur cycle during periods with a marine sulfate reservoir substantially smaller than the modern (Kah et al., 2016). We recognize that vertical gradients in seawater $\delta^{13}C$ exist that are dynamically maintained by the 'biological pump', all of which are superimposed on the $\delta^{13}C_{carb}$ signal; however, because this study focuses on shallow water settings that are not directly connected to deep water bodies, we simplify the oceanic carbon cycle as a single reservoir. If $\delta^{13}C$ or $\delta^{34}S$ measured from stratigraphic successions can be reasonably determined to preserve a seawater value, then these $\delta^{13}C$ and $\delta^{34}S$ trends can be interpreted to reflect changes to the global carbon and sulfate reservoirs. Under anoxic conditions, perhaps as the oxygen chemocline impinges upon the seafloor, burial rates of organic carbon and pyrite will increase, ultimately increasing seawater $\delta^{13}C$ and $\delta^{34}S$ to create parallel positive excursions with continued anoxia and deposition. [Anoxia in this study, as inferred by positive $\delta^{13}C$ and $\delta^{34}S$ excursions, refers to widespread enhanced organic carbon and pyrite burial under reducing conditions, which may also include euxinic conditions if sulfide was present in the water column.]

The inference that $\delta^{13}C$ and $\delta^{34}S$ excursions reflect anoxia on a global scale is reinforced when these isotope proxies are coupled with independent data that are thought to record local redox changes in the overlying water column (Gill et al., 2011; Li et al., 2010). Iodine measured from carbonate rocks and sediment (I/Ca) is used as a proxy for more localized upper ocean redox conditions (Hardisty et al., 2017, 2014, Lu et al., 2016, 2010; Zhou et al., 2015) and provides an opportunity to compare with global isotope proxies when measured from the same carbonate sample (micrite, here; cf. Owens et al., 2017; Zhou et al., 2015). Lime mud (micrite) can form either by the disintegration of skeletal or algal material or as a direct precipitate in the water column (Tucker and Wright, 1990), thus capturing a seawater signature, when confirmed with petrography to preserve a primary fabric.

2.3. I/Ca as a local redox proxy

Iodine has two stable inorganic forms in seawater, the oxidized form iodate (IO_3^-) and the reduced form iodide (I^-), and has a high reduction potential comparable to O_2/H_2O (Lu et al., 2010). Carbonate production in the water column incorporates IO_3^- into the carbonate structure but excludes I^- (Lu et al., 2010). Thus, iodine concentrations of bulk carbonate can be used to estimate the iodate concentrations in the water column. Bulk carbonate I/Ca has been referred to as a local redox proxy for upper ocean conditions, based on (1) ample iodine speciation data of modern seawaters (e.g. Rue et al., 1997), (2) I/Ca of modern foraminifera shells across a range of upper ocean oxygenation conditions (Lu et al., 2016), and (3) paleoceanographic reconstructions of ocean deoxygenation events (e.g. Zhou et al., 2015, 2014). Geochemically, a global proxy produces more or less similar trends in different parts of world oceans, whereas a local proxy can show different values and trends at different locations.

The long residence time of iodine (~300 kyr) leads to generally uniform total iodine concentrations in modern ocean (Campos et al., 1999). However, the speciation changes of iodine in the upper ocean are very local phenomenon, which can be strongly affected by the presence or absence of oxygen minimum zones (OMZs) (Rue et al., 1997) with some relatively minor influence of productivity (Chance et al., 2010). Iodate reduction in OMZs results in a sharp decrease in $[IO_3^-]$, locally in the upper ocean.

Such an OMZ-type iodate profile will be captured by calcium carbonate formed in the shallow water column. Core-top (modern) planktonic foraminifera shells (Lu et al., 2016) record near zero I/Ca above shallow OMZs in the equatorial Pacific, and record notably higher values (>3 μmol/mol) at well-oxygenated locations, which is consistent with seawater iodine speciation studies.

Applications in ocean de-oxygenation events have further confirmed the use of I/Ca as a local proxy. Multiple coeval records of I/Ca from different parts of proto-Atlantic basin demonstrate spatial patterns of I/Ca values during the Mesozoic Oceanic Anoxic Event 2 (OAE 2), with clearly higher values at an oxygen 'oasis' simulated in an Earth System Model (Zhou et al., 2015). Foraminiferal studies of the Paleocene–Eocene Thermal Maximum also demonstrate that local redox conditions in either upper or bottom waters, as recorded by I/Ca in planktonic and benthic species, respectively, are most consistent with multi-proxy comparison and data-model comparison (Zhou et al., 2016, 2014). Therefore, I/Ca is a promising independent tool to evaluate paleo-redox, complementary to those more established proxies for global redox changes.

Constraints on iodine fluxes in the modern ocean (Lu et al., 2010) suggest iodine is mostly recycled in modern seawater but burial with organic matter could be an important sink over long timescales. However, a recent study of organically bound iodine in black shale during Mesozoic OAEs does not suggest ubiquitous drawdown of iodine during large scale ocean anoxia (Zhou et al., 2017). This likely reflects the decrease in iodate concentrations in bottom water during OAEs, leading to less efficient burial of organically bound iodine.

3. Methods

3.1. Sampling and location

The three sections studied here (Ibex area, UT, Shingle Pass, NV, and Meiklejohn Peak, NV) have been previously studied for their biostratigraphic (e.g. Adrain et al., 2014; Ethington and Clark, 1981; Hintze, 1951; Sweet and Tolbert, 1997) and $\delta^{13}C$ chemostratigraphic context (Edwards and Saltzman, 2016, 2014; Saltzman et al., 2015). Geochemical analyses in this study were performed on from samples collected from a composite section in Ibex (Lava Dam North, B-Top, and C-1965 sections of Hintze, 1973), the 85WA section at Shingle Pass (Edwards and Saltzman, 2014; Sweet and Tolbert, 1997), and the southwestern section at Meiklejohn Peak (Ross, 1964). Thin sections were made from representative facies to investigate the potential for diagenetic overprints in transmitted light microscopy and cathodoluminescence (CL) using a RELIOTRON cold cathode system at Appalachian State University.

3.2. Geochemistry

New $\delta^{13}C_{carb}$ data presented here (Table S1; supplementing existing data with higher resolution in all three sections presented in Edwards and Saltzman, 2016, 2014) were measured from previously collected lime mudstone samples using standard methods for stable carbon isotopic analysis (cf. Edwards and Saltzman, 2014) and reported in per mil (‰) using delta notation relative to the Vienna Pee Dee Belemnite standard (V-PDB). We used a modified CAS-extraction protocol (Wotte et al., 2012) designed to more effectively remove non-primary sulfate and maximize the chances of obtaining the most environmentally meaningful $\delta^{34}S_{CAS}$ values. Previous studies used a single rinse of 10% NaCl to dissolve and remove any non-CAS sulfate that may be adsorbed to carbonate minerals or in the form of evaporite minerals (including preliminary $\delta^{34}S_{CAS}$ data presented in Saltzman et al., 2015), but recently Wotte et al. (2012) showed that a single NaCl rinse did not completely remove non-target sulfate. Here, carbonate powders, usually 40–50 g, were rinsed in 500 mL of 10% NaCl for 12 h at least three times until the filtered supernatant of the final rinse yield no $BaSO_4$ precipitate when 1 M $BaCl_2$ was added. Samples were then rinsed three times with 500 mL of deionized water before dissolution in 6 N HCl. Dissolved samples were filtered within 2 h of acidification and the insoluble residues were rinsed and dried for pyrite-S extraction. Approximately 1–2 mL of 1 M $BaCl_2$ was added to the filtered solution and allowed to form $BaSO_4$ for 2–4 days.

Dried insoluble residues were processed for pyrite-S using the chromium-reducible sulfide method. Residue samples (1–2 g) were reacted with 25 mL of 2 M chromium (II) chloride and 25 mL 6 N HCl under a nitrogen atmosphere and stirred on a hotplate at 183 °C for at least 2 h. Evolved SO_2 gas was passed through a water trap prior to reacting with 0.1 N $AgNO_3$ to form a Ag_2S precipitate, which was rinsed, dried, and weighed.

$BaSO_4$ and Ag_2S samples were processed for isotopic analysis at Washington University in St. Louis. Samples were combusted with excess V_2O_5 using a 4010 ECS Costech Elemental Analyzer coupled to a Thermo Delta V Plus Isotope Ratio Mass Spectrometer via Conflo IV. Values are reported in per mil (‰) using delta notation ($\delta^{34}S$) relative to the Vienna Canyon Diablo Troilite (V-CDT) (Table S1). All runs contained internal laboratory standards calibrated to international standards IAEA-S1, -S2, and -S3 where the average reproducibility (1σ) of standards in a single run was <0.3‰.

Processing and analytical methods for I/Ca followed those of Zhou et al. (2015) and are briefly outlined here. Between 2–5 mg of carbonate powders were rinsed with DI water, prior to complete dissolution in 3% nitric acid. Solutions were separated from insoluble residues via centrifuge and diluted for analysis using inductively coupled plasma–mass spectrometry (ICP-MS). Samples were analyzed on a quadrupole ICP-MS (Bruker M90) at Syracuse University using 0.1% tertiary amine (to aid in iodate stabilization) and internal standards. Pure potassium iodate was dissolved and diluted for a set of calibration standards where the ^{127}I sensitivity was 80–100 kcps for the 1 ppb standard. Precision of ^{127}I was typically better than 1%. Long-term accuracy was guaranteed by repeated measurement of the reference material JCp-1 (Lu et al., 2010), and the detection limit of I/Ca was about 0.1 μmol/mol. Mg was not measured in this study and all iodine concentrations are normalized to Ca concentration only.

4. Results

$\delta^{13}C_{carb}$, $\delta^{34}S_{CAS}$, $\delta^{34}S_{py}$ (Table S1), and I/Ca (Table S2) profiles from the three sections studied here show similar stratigraphic trends for each geochemical record across the Skullrockian–Stairsian boundary (Figs. 2–4). The $\delta^{13}C_{carb}$ signal is the most robust and is clearly defined by a pronounced positive excursion in each section, despite some anomalies within the flat pebble conglomerate facies at Ibex, with similar pre-excursion baselines (−0.5 to −0.8‰) and peak $\delta^{13}C_{carb}$ values (+1 to +1.5‰). Ibex shows the strongest evidence for coupled $\delta^{13}C$ and $\delta^{34}S$ variations among the three sections, wherein $\delta^{13}C_{carb}$ and $\delta^{34}S_{CAS}$ (but less so for $\delta^{34}S_{py}$) exhibit a positive excursion starting in the uppermost House Limestone and continuing into the Fillmore (Fig. 2). This coupling, however, is less apparent at Shingle Pass where $\delta^{13}C_{carb}$ and $\delta^{34}S_{CAS}$ increase together, but $\delta^{34}S_{CAS}$ remains relatively positive while $\delta^{13}C_{carb}$ returns to baseline values after the excursion (Fig. 3). Despite a lower sampling density at Meiklejohn Peak, $\delta^{13}C_{carb}$ and $\delta^{34}S_{CAS}$ show evidence of being coupled where peak isotope values co-occur within the excursion interval (Fig. 4). A large shift in $\delta^{34}S_{CAS}$ values before the excursion at Meiklejohn Peak obscures a clear baseline value (see Discussion section be-

low for possible diagenetic effects on $\delta^{34}S_{CAS}$), but pre-excursion $\delta^{34}S_{CAS}$ values are ~33‰ at Shingle Pass and Ibex.

$\delta^{34}S_{py}$ values exhibit greater sample-to-sample variability compared to $\delta^{34}S_{CAS}$, in some instances up to 20‰, and are only weakly similar to $\delta^{13}C_{carb}$ and $\delta^{34}S_{CAS}$ trends during the positive $\delta^{13}C_{carb}$ and $\delta^{34}S_{CAS}$ excursions. Whereas the most positive $\delta^{34}S_{py}$ values occur during the positive $\delta^{13}C_{carb}$ and $\delta^{34}S_{CAS}$ excursions at Ibex (+34.8‰) and Shingle Pass (+35.1‰), there is not a clear positive $\delta^{34}S_{py}$ excursion across the Stairsian-Skullrockian boundary. A single positive $\delta^{34}S_{py}$ value at Meiklejohn Peak (+21.7‰; Fig. 4), however, occurs during the $\delta^{13}C_{carb}$ and $\delta^{34}S_{CAS}$ excursions, but more detailed sampling across this interval is needed to more definitively assess a parallel relationship among $\delta^{13}C$ and $\delta^{34}S$ trends at this section. No apparent stratigraphic trends in $\Delta^{34}S$ are observed across the $\delta^{34}S$ excursion in any section ($\Delta^{34}S$ represents the difference between $\delta^{34}S_{CAS}$ and $\delta^{34}S_{py}$; $\Delta^{34}S = \delta^{34}S_{CAS} - \delta^{34}S_{py}$).

Cross-plots between $\delta^{13}C$ and $\delta^{34}S$ vs. I/Ca values show an inverse but weak correlation ($r^2 = 0.03$–0.39 and 0.03–0.10, respectively) across the Skullrockian–Stairsian boundary where the lowest I/Ca values occur prior to or during the onset of the isotope excursions (Fig. S1). At Shingle Pass and Meiklejohn Peak I/Ca ratios fall to zero during the $\delta^{13}C_{carb}$ excursion, but at Ibex I/Ca reaches zero below the onset of the $\delta^{13}C_{carb}$ excursion and fluctuates between 0.5–0.25 μmol/mol throughout and after the excursions. Correlations between $\delta^{13}C_{carb}$ and I/Ca at Shingle Pass and Meiklejohn Peak are weak ($r^2 = 0.39$ and 0.10, respectively), but $\delta^{13}C_{carb}$ and I/Ca at Ibex show no correlation ($r^2 = 0.03$). $\delta^{34}S_{CAS}$ vs. I/Ca shares a negative but weak correlation in all sections during the $\delta^{13}C_{carb}$ excursion (Fig. S1).

5. Discussion

5.1. Potential diagenetic alteration effects of geochemical data

5.1.1. Petrography and cathodoluminescence microscopy

Thin section study shows that the fragmentary nature of several skeletal fragments suggests some transport has occurred (Fig. 5), questioning whether these facies accurately reflect environmental conditions in the location where deposition occurred. Most of the samples studied herein, however, are primarily lime mudstone facies with some siliciclastic clay laminae, which we interpreted to record low energy conditions that allowed for carbonate mud to accumulate near the site of precipitation in the water column. Carbonate mud that comprises matrix between skeletal fragments was also likely transported with bioclasts. We assume that transport distances were not far from their origin (i.e. parautochthonous) in this shallow subtidal environment (below fair-weather wave base) and that only during infrequent storm events did sediment reworking and transport occur in these settings (cf. Ross et al., 1989). Therefore, we infer that any primary geochemical signatures preserved in these carbonates most likely reflect seawater chemistry at, or near the site of carbonate formation.

Thin sections are routinely used to study petrographic fabrics of carbonate grains, matrix, and cements using transmitted light and cathodoluminescence (CL) microscopy to screen for diagenetic features (e.g. Hiatt and Pufahl, 2014). Progressive alteration and recrystallization can increase Mn and Fe concentrations of carbonates (Brand and Veizer, 1980), given porewaters were anoxic and contained dissolved Mn^{2+} and Fe^{2+}, two metals that most commonly affect luminescence in thin section. The excitation of trace amounts of Mn (>~20 ppm) in calcite causes carbonate minerals to luminesce in yellow, orange, and red colors (Hiatt and Pufahl, 2014, and refs. within). Iron, however, is a CL quencher and concentrations ≥200 ppm in carbonate minerals will typically luminesce as dark red, brown, or not at all with increasing amounts, despite an abundance of Mn (Hiatt and Pufahl, 2014).

Thin section study using CL reveals that most facies studied herein have experienced a similar degree of late burial diagenesis where most skeletal grains and matrix have similar dull red–orange luminescence (Fig. 5). Samples from below the $\delta^{13}C_{carb}$ excursion (MP 291), at the peak (B-TOP 7416), and above (SP 7553) all show similar dull luminescent deep red colors of lime mudstone intraclasts and mud matrix in CL, consistent with Mn- and Fe-bearing carbonate phases. Trilobite fragments show early stages of silicification along boundaries, which are clearly evident as non-luminescent crystals in CL (white arrows in Figs. 5B and 5D). Evidence for early meteoric dissolution or cementation is absent (e.g. vadose or phreatic cements coating grains), but some echinoderm fragments have thin luminescent cements that likely reflect early (meteoric?) cementation. In general, most carbonate phases (grains, matrix, early cements) appear to have experienced a similar late burial diagenetic overprint, evidenced by silicified trilobite fragments and indistinguishable intraclast boundaries with matrix (Fig. 5D). We see no evidence in hand sample or in thin section indicating more intense diagenetic alteration in intervals marked by near zero I/Ca values from any of the three sections examined in the present study. We do not rule out the possibility that diagenesis was not uniform across the entire section at all three locations and instead we rely on the multi-proxy approach to reconstruct the redox history.

5.1.2. Assessment of diagenesis on geochemical trends

Stable isotope trends and trace element concentrations are used herein to assess the degree of diagenetic alteration prior to any interpretation of their environmental significance. For example, during recrystallization impurities in the calcite crystal lattice (i.e. sulfate and iodate) will be removed to minimize crystal energy, given porewaters have lower trace element concentrations than the fluids from which the calcite precipitated. With progressive recrystallization, concentrations of sulfate ([CAS]) and iodate (I/Ca) should correlate because both are expected to decrease with increasing alteration. Diagenetic recrystallization can also impact $\delta^{13}C_{carb}$, $\delta^{34}S_{CAS}$, and $\delta^{18}O_{carb}$ via fluid interaction and incorporation of these lighter isotopes from meteoric waters, ultimately derived from the oxidation of reduced carbon (soil organic matter) or sulfur (sedimentary pyrite) from surrounding rocks. $\delta^{34}S_{CAS}$ is particularly susceptible to yielding anomalously low values because partial or complete oxidation of sedimentary pyrite can occur either prior to lithification, during burial diagenesis, or in the laboratory during CAS extraction. If pyrite oxidation that releases ^{32}S-enriched sulfate into porewater occurs prior to lithification under (partial) closed system conditions, this scenario could give rise to low $\delta^{34}S_{CAS}$ values as pore-filling calcite cement incorporates ^{32}S-enriched sulfate as CAS. If original CAS concentrations were low (which is true of several samples in this study), then mixing of pore-filling spar with a bulk sample can produce anomalously depleted bulk $\delta^{34}S_{CAS}$ values relative to less altered surrounding rocks.

The formation of sedimentary pyrite begins with the microbial reduction of seawater sulfate, imparting a fractionation effect of ~30–70‰ in most natural environments, but several biotic and abiotic oxidation and reduction processes can be involved prior to the formation of pyrite (Canfield, 2001 and refs. within). If pyrite remains pristine after formation in sediment, then $\delta^{34}S_{py}$ trends should parallel $\delta^{34}S_{CAS}$ trends because $\delta^{34}S_{CAS}$ is thought to record the $\delta^{34}S$ of seawater sulfate, the ultimate source of most pyrite sulfur. However, because of the wide range in biological fractionation during microbial sulfur cycling (e.g. Leavitt et al., 2013; Sim et al., 2011), there is considerable additional variation superimposed on $\delta^{34}S_{py}$ signals. As such, in this study we emphasize

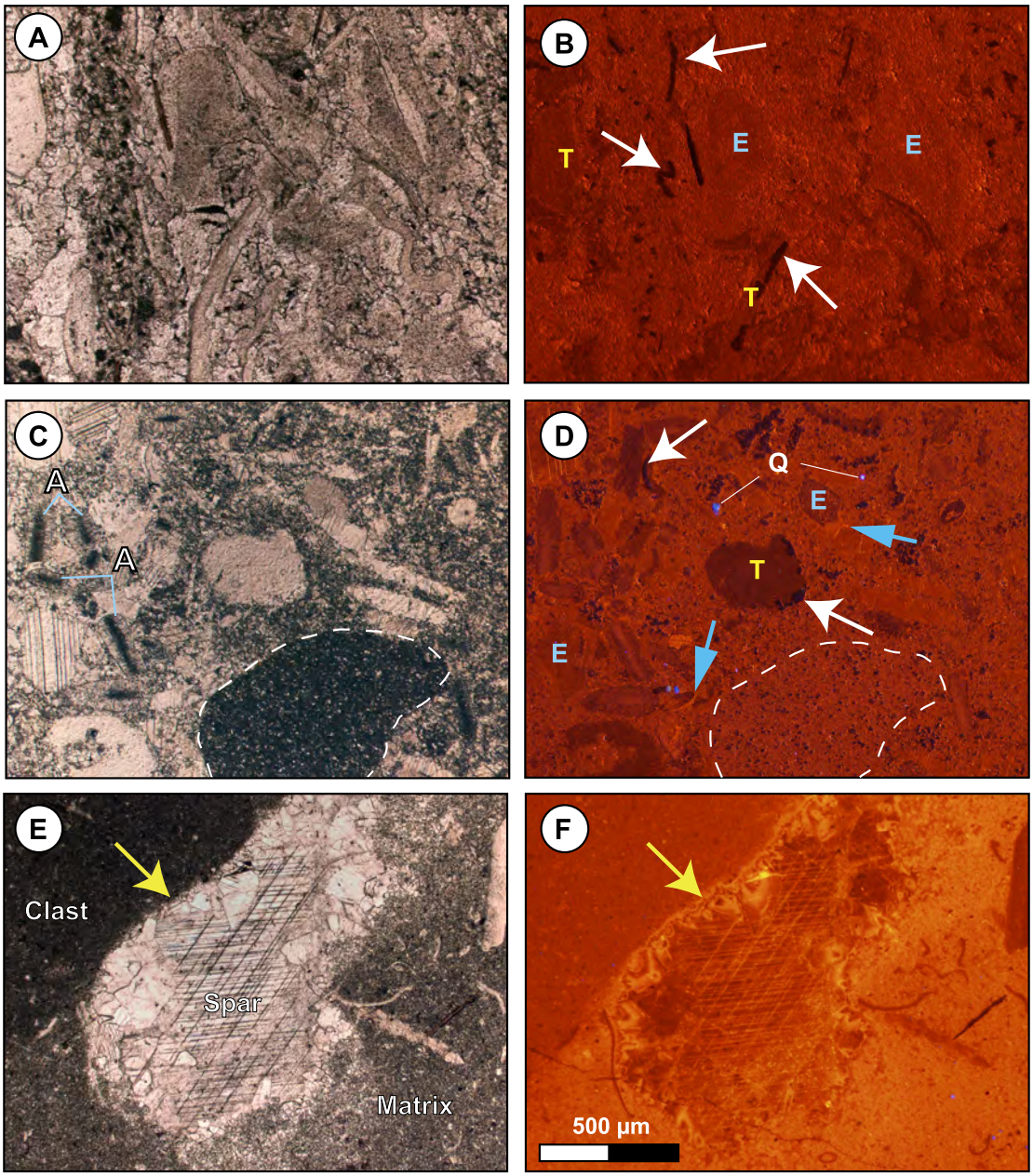

Fig. 5. Photomicrographs of representative of lithologies sampled in this study. **A** and **B**) B-TOP 7416 in plane-polarized transmitted light (A) and in cathodoluminescence (CL) (B). B-TOP 7416 varies between mudstone–wackestone (wackestone shown here with trilobite (T) and echinoderm (e) fragments, suggestive of some transport prior to burial). CL reveals nearly uniform dully-luminescent red–orange burial calcite cement that comprises most of the sample and overprints grains and matrix, with the exception of non-luminescent silica that has partially replaced trilobite fragments (arrows). B-TOP 7416 occurs at the peak of the $\delta^{13}C_{carb}$ excursion (star in Fig. 2). **C** and **D**) SP 7553 in plane-polarized transmitted light (C) and in CL (D). SP 7553 is a mixed assemblage of mudstone intraclasts (white dashed outline) and wackestone with trilobite (T), an unidentified calcifying algae (A), and echinoderm (E) fragments. SP 7553 is similarly predominantly dully luminescent with replacement silica (arrows) and detrital blue quartz in CL (Q). A pervasive late burial red–orange calcite cement overprints most of the sample, but vestiges of an early seafloor cement within echinoderm fragments exist, as well as a thin coating of yellow–orange cement (high Mn, low Fe; blue arrows). SP 7553 occurs above the $\delta^{13}C_{carb}$ excursion (star in Fig. 3). **E** and **F**) MP 291 in plane-polarized transmitted light (C) and in CL (D). MP 291 has mixed carbonate phases of mudstone intraclasts, trilobite-bearing lime mud matrix, and pore-filling blocky calcite spar. The intraclasts in MP 291 are dully luminescent surrounded by more brightly luminescent red–orange lime mud matrix. Calcite cement grew in several stages, first with an isopachous bladed spar phase (yellow arrows) followed by a single pore-filling phase with twinning. MP 291 occurs below the $\delta^{13}C_{carb}$ excursion (star in Fig. 4). Scale bar applies to all images. CL images taken at 7.0–8.0 kV beam intensity with 0.5 mA beam current.

trends in $\delta^{34}S_{CAS}$ as a more meaningful indicator of environmental change (i.e. pyrite burial during anoxic or euxinic conditions) rather than $\delta^{34}S_{py}$-based trends.

The presence of pyrite can also impact the CAS record (Marenco et al., 2008; Wotte et al., 2012). Because pyrite is relatively reactive near the oxygenated surface environment, partial oxidation can occur either during burial, post-burial if exposed to oxidizing fluids, or in the laboratory if exposed to highly acidic or oxidizing conditions during CAS extraction (Marenco et al., 2008; Wotte et al., 2012), with potential impact on the $\delta^{34}S_{CAS}$ record (e.g. Jones and Fike, 2013). Indeed, the variations observed in $\delta^{34}S_{CAS}$ between the different sections presented here argue that additional factors beyond simple changes in overall marine seawater $\delta^{34}S_{SO_4}$ must have variably impacted the observed $\delta^{34}S_{CAS}$ values.

Geochemical trends suggest that some carbonates in this study have been impacted by diagenesis, but the degree of alteration appears to be relatively uniform within individual sections and insuf-

ficient to have completely reset what appear to be primary seawater trends. Partial pyrite oxidation prior to cementation may have occurred at Meiklejohn Peak where $\delta^{13}C_{carb}$ and $\delta^{34}S_{CAS}$ trends appear to briefly and quickly decouple below the $\delta^{13}C_{carb}$ excursion (Fig. 4). Three $\delta^{34}S_{CAS}$ values from fine-grained laminated lime mudstone are anomalously low relative to neighboring values, also giving the appearance that $\Delta^{34}S$ is increasing throughout the lower part of this section. These samples are not ideal for CAS analysis due to their high amount of insoluble clay mineral residue (e.g. MP-294 is only 66.7% $CaCO_3$) that may have acted as conduits for increased porewater interaction along laminae to partially oxidize pyrite in the surrounding carbonate. Petrography of one of these samples (MP-291; Figs. 5E and 5F) shows calcite spar-filled pores lined with several stages of calcite growth. It may be possible that rocks immediately below the $\delta^{13}C_{carb}$ excursion instead record a transient 15‰ decrease in ambient seawater sulfate $\delta^{34}S$, followed by a return to a baseline value of ~30‰ prior to a modest ~5‰ positive $\delta^{34}S_{CAS}$ excursion (Fig. 4). However, the fact that a similar 15‰ negative excursion is not present in the other measured sections argues against these data reflecting seawater sulfate.

Cross plots between sulfate and iodate concentrations suggest that diagenesis was not severe enough to completely remove these lattice-bound compounds (Fig. S2). CAS and I/Ca concentrations from Ibex and Shingle Pass have almost no correlation ($r^2 = 0.02$ and 0.01, respectively), indicating that diagenetic removal of sulfate and iodate during recrystallization was likely not responsible for variations in [CAS] and I/Ca. At Meiklejohn Peak, there is a weak correlation between [CAS] and I/Ca ($r^2 = 0.36$), suggesting diagenetic alteration may have played a role in these trends, also consistent with some anomalous $\delta^{34}S_{CAS}$ values. Diagenetic alteration of carbonate via meteoric recrystallization, neomorphism of aragonite to low Mg-calcite, or dolomitization tends to only lower I/Ca values (Hardisty et al., 2017). However, meteoric diagenesis on the same set of samples altered [CAS] significantly (Gill et al., 2008), but preserved the primary I/Ca signals in some cases (Hardisty et al., 2017). Such a decoupling between [CAS] and I/Ca during diagenesis suggests that the weak correlation between [CAS] and I/Ca at Meiklejohn Peak do not conclusively indicate alterations of I/Ca trend.

Overall, a diagenetic overprint likely contributed to the variability of some geochemical data (evidenced by some anomalously low $\delta^{18}O_{carb}$ at Shingle Pass and $\delta^{34}S_{CAS}$ values at Meiklejohn Peak (Fig. S1) and highly variable $\delta^{34}S_{py}$ in all sections). Regardless, diagenesis does not appear to be a main driver of the observed geochemical trends, which is also supported by petrography and hand sample analysis.

5.2. Geochemical evidence for anoxia

Parallel $\delta^{13}C$ and $\delta^{34}S$ excursions in the rock record have traditionally been used as proxy evidence for global anoxic events associated with increased burial of organic carbon and pyrite, respectively (Adams et al., 2010; Gill et al., 2011; Gomes et al., 2016; Owens et al., 2013). Iodine concentrations in carbonate rocks (I/Ca) are thought to primarily reflect more local redox conditions in upper ocean (Zhou et al., 2015). If the local extinction event at Ibex was caused by the expansion of widespread anoxia (cf. Saltzman et al., 2015), then both the I/Ca proxy and $\delta^{13}C$ and $\delta^{34}S$ trends should show parallel evidence anoxia. Thus, this relationship can be used to explore potential spatial and temporal relationships between global and local signals.

Paired $\delta^{13}C$ and $\delta^{34}S$ excursions measured across the Skullrockian–Stairsian boundary in the Great Basin region support the hypothesis that organic and pyrite burial rates had increased under reducing conditions at this time, consistent with the idea that anoxia (likely euxinia) was either widespread globally or long-lived in the shallow marine environments studied herein. Conodont biozones that bracket this Tremadocian event, however, indicate that this anoxic period lasted less than 50 kyr as calibrated to the 2012 Geologic Time Scale (Cooper and Sadler, 2012). These biozones (*Rossodus manitouensis*, Low Diversity Interval, and *Macerodus dianae*; Fig. 2) are inferred to be less than ~0.15 Myr in duration, significantly shorter than the >2 Myr for the adjacent biozones, although there are few direct radiometric age dates to support this assumption. If instead an average sedimentation rate, for example 5–10 mm/kyr (similar to some estimates of pelagic sedimentation rates along Tethyan margins Lowrie and Alvarez, 1984), is used to estimate the duration of anoxia as represented by the onset of the $\delta^{13}C$ excursion until the peak (~15 m at Ibex), then the duration would be 1.5–3 Myr and similar to the late Cambrian SPICE event (Saltzman et al., 2011). A duration of 50 kyr for this anoxic event also appears to be too short when considering that the coupling of $\delta^{13}C$ and $\delta^{34}S$ trends indicates that this event must have lasted longer than the residence time of sulfur (~10^6 yr), which is much longer than the residence time of dissolved inorganic carbon (10^5 yr) in the ocean. Furthermore, the amount of pyrite burial that would be required to produce the observed ~15‰ $\delta^{34}S_{CAS}$ excursion is unrealistic for a 50 kyr interval. A first-order calculation using a lower estimate for the sulfate reservoir size (2.6×10^{18} mol S, equal to 2 mM) thought possible for the Early Ordovician (Kah et al., 2016) would require pyrite burial rates to increase by at least 12 times with 70–90% of sulfur removal from the sulfate reservoir in the form of pyrite in order to produce a 15‰ $\delta^{34}S_{CAS}$ excursion (Fig. S3). Taking the duration of 50 kyr at face value, this would require that the observed $\delta^{13}C$ and $\delta^{34}S$ signals are primarily responding to an environmental signal distinct from changes in their respective marine reservoirs. While this is not the standard interpretation of these isotopic records, some amount of local environmental influence (be it during deposition or subsequently during diagenesis) is required by the stratigraphic differences that are observed in $\delta^{13}C_{carb}$ and $\delta^{34}S_{CAS}$ between the different sections presented here.

Evidence for localized anoxia is based on near zero I/Ca values coincident with the $\delta^{13}C$ and $\delta^{34}S$ excursions, particularly at Shingle Pass and Meiklejohn Peak (Figs. 3 and 4). These two sites were located at relative deeper depths and further away from the shore. I/Ca records at such locations arguably are more suitable to be compared with the global proxies (C and S). The decrease of I/Ca values during an oceanic de-oxygenation event is driven by the shoaling of subsurface reducing zone, whereas the wind-mixed layer of surface water remains well-oxygenated. The downward supply of dissolved O_2 by wind mixing is controlled by atmospheric dynamics and can be easily decoupled from global biogeochemical perturbations. Therefore, the I/Ca trends at deeper sites may be less influenced by mixed-layer processes and show better synchronization with $\delta^{13}C$ and $\delta^{34}S$ excursions. For this reason. I/Ca data from Ibex are discussed separately below and are excluded from the composite section for clarity in comparing I/Ca with the $\delta^{13}C$ and $\delta^{34}S$ records (Fig. 6). A LOESS regression line passed through a composite of all $\delta^{13}C$ and $\delta^{34}S$ data more clearly shows the parallel nature of global and local proxy evidence for anoxia (Fig. 6). Taken together, the behavior of $\delta^{13}C$, $\delta^{34}S$ and I/Ca in these sections demonstrate similarities with OAE 2, which is a classic example of widespread anoxia with positive $\delta^{13}C$ and $\delta^{34}S$ excursions (Owens et al., 2017, 2013; Zhou et al., 2015).

Regardless of the broad consistency between the composite I/Ca and global proxies, some unexpected observations in the records require further discussion. At Ibex, near zero I/Ca values precede the $\delta^{13}C$ and $\delta^{34}S$ excursions and main extinction interval (Figs. 2 and 6), leading to the lack of correlation between low I/Ca and the phase-lagged high $\delta^{13}C$ and $\delta^{34}S$ values (Fig. S1). Though diagenesis can produce low I/Ca via recrystallization or

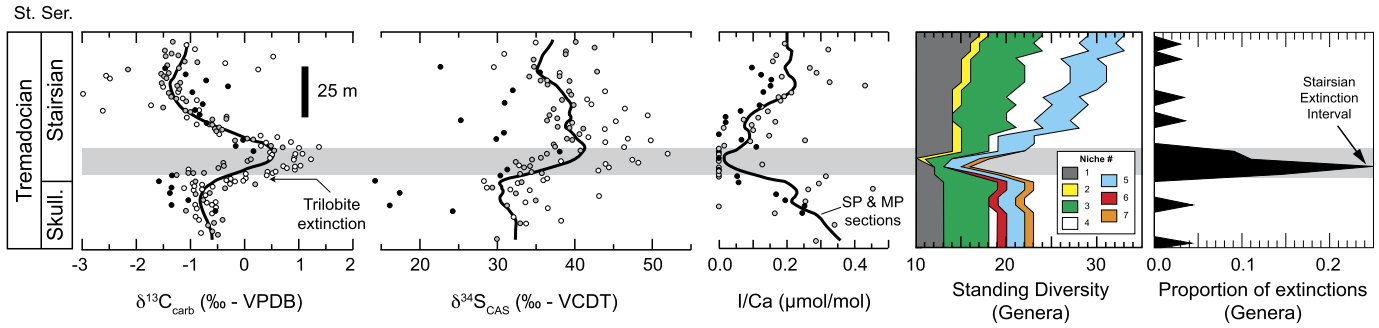

Fig. 6. Composite of geochemical data compared with paleontological data from Ibex across the Skullrockian–Stairsian boundary. LOESS smoothing lines ($\alpha = 0.2$) show the timing of the paired positive $\delta^{13}C$ and $\delta^{34}S$ excursions correlate well with the interval of local anoxia (gray box) based on the I/Ca minima from Shingle Pass and Meiklejohn Peak (see main text for why I/Ca data from Ibex are omitted here). Onset of isotope excursions and I/Ca minima coincides with a major extinction interval of generic diversity and base-Stairsian trilobite extinction interval of Adrain et al. (2014). Standing diversity trends of various taxonomic groups, and proportion of extinction of genera per 5-m bin. Taxonomic data are presented in Tables S3 and S4. Niches defined in Table S4 and represented by the following taxonomic groups: 1) conodonts, 2) graptolite and agnostid trilobite, 3) trilobites – deposit feeding, 4) trilobite – predatory, 5) brachiopod – benthic, sessile, 6) brachiopod – benthic, unattached, and 7) brachiopod – infaunal.

dolomitization (e.g. Hardisty et al., 2017), samples with low I/Ca at Ibex below the $\delta^{13}C$ and $\delta^{34}S$ excursions and extinction do not show clear evidence of alteration in hand sample or in thin section by optical or CL analysis. Nor do these samples have significantly lower [CAS] relative to surrounding samples, and $\delta^{13}C$ and $\delta^{18}O$ values are invariant across this interval. Furthermore, there is no apparent diagenetic difference between samples with low I/Ca and high I/Ca in samples from the same shallow subtidal depositional facies. These facies are fossiliferous and suggest (at least episodically) oxygenated conditions during deposition. It is important to emphasize that low I/Ca values recorded at this shallow site do not indicate anoxia in the seafloor habitat of animals, but instead reflect the presence of O_2-depleted water at shallow depth. This scenario is analogous to modern OMZs recorded in the I/Ca of planktonic foraminifera living directly above the OMZ (Lu et al., 2016). The re-oxidation of iodide can be slow (Chance et al., 2014) during the mixing between subsurface low O_2 water and the surface water, which allows very shallow carbonate to record the signature of a subsurface O_2-depletion. These near-zero I/Ca values may suggest a short-lived episode of local coastal hypoxia at Ibex prior to the global signature. Similar findings are reported for OAE 2 (Ostrander et al., 2017; Owens et al., 2017; Zhou et al., 2015) since local organic carbon burial (and anoxia) must have increased prior to any impact on global $\delta^{13}C$. One trilobite genus (*Clelandia*) did go extinct locally at Ibex where I/Ca values reach near zero, possibly in response to this hypoxic event (Fig. 6), although this apparent extinction may be due to preservation biases or low sampling resolution throughout this interval.

5.3. Biodiversity crisis caused by anoxia?

Preservational biases do not play an important role across the House–Fillmore interval as the majority of reported taxonomic occurrences are preserved as either silicified trilobites or phosphatic conodonts (Adrain et al., 2014; Ethington and Clark, 1981). Sampling biases exist, however, such that reported data are of taxonomic groups that are typically robust and resistant to destruction during burial or easily identified, unlike mollusks whose aragonite shells have since dissolved or echinoderm plate fragments of unknown affinity. Thus, the available paleontological data provide a cursory overview of the ecological impact at Ibex and exclude effects to soft-bodied faunas.

Biodiversity data at Ibex (Tables S3 and S4) compiled from the literature (e.g. Adrain et al., 2014; Ethington and Clark, 1981; Hintze, 1951) record a major extinction at approximately the same interval as the onset of the isotope excursions (Fig. 6). Standing diversity (taxa existing throughout an interval; cf. Bambach et al., 2004) decreased from 23 to 16 genera over 10-m-thick interval across the House–Fillmore interval, representing a 30% loss of generic diversity (Fig. 6). Diversity recovers to pre-extinction levels at or just after the $\delta^{13}C_{carb}$ excursion peak and continues to gradually rise throughout the end of the excursion. These preliminary trends indicate that the Ibex biota were affected by the same event that caused the geochemical perturbations.

A 30% drop of standing generic biodiversity occurs across the Skullrockian–Stairsian boundary at Ibex (Fig. 6), coincident with $\delta^{13}C$ and $\delta^{34}S$ evidence for anoxia, but less so for I/Ca. Taxa from a range of niches were affected by this mass extinction, from nekto-benthic trilobite predators to sessile epifaunal and infaunal brachiopods, but benthic deposit-feeding trilobites were most severely impacted (Fig. 6). Benthic-dwelling taxa experienced the highest extinction rates (40%) across the House–Fillmore interval, whereas pelagic and nektic taxa (i.e. conodonts) had only a 23% extinction rate. Higher extinction rates among benthic taxa are consistent with the expansion of anoxic bottom waters during a relative sea-level rise above a "brown siltstone" lowstand deposit (Saltzman et al., 2015). The anoxic interval, as defined by the I/Ca minimum at Shingle Pass and Meiklejohn Peak (Fig. 6), also occurs at the same interval as the mass extinction. It is possible that anoxia caused inhospitable conditions to persist at Ibex that drove marine life away to occupy nearby oxygenated environments. Regardless of whether anoxia was the actual kill mechanism, this anoxic event is at least a symptom of the ultimate cause because species go extinct locally and are not identified in the overlying strata. Biodiversity levels at Ibex appear to recover during the isotope excursions and may record a return to oxygenated waters locally while the global $\delta^{13}C$ and $\delta^{34}S$ signals would require $>10^5$ yr to recover to pre-excursion values. The Ibex section preserves fluctuating and generally increasing I/Ca values (Fig. 2) during the anoxia interval inferred from other deeper sections (Fig. 6), which may be local recovery from anoxia predating regional and global changes, consistent with the biodiversity data. Biodiversity quickly returns to pre-extinction levels by the peak of the $\delta^{13}C$ and $\delta^{34}S$ excursions (Fig. 6), suggesting a return to oxic conditions here locally, and continue to rise until the last major anoxic (extinction) event (North American Tulean Stage; Saltzman et al., 2015) of the Early Ordovician. When this Stairsian mass extinction is placed in the context of geochemical evidence it reinforces the view that anoxia was the central cause of the extinction, the (near) absence of iodine in carbonate rocks from this interval, and $\delta^{13}C$ and $\delta^{34}S$ excursions as a result of organic and pyrite burial that affected the global carbon and sulfate reservoirs, respectively. As frequent, recurrent anoxic events in shallow shelf environments end before the Middle Ordovician, marine life was able to diversify and fill new ecospace for millions of

years in a relatively stable environment until the end Ordovician mass extinction.

6. Conclusions

Geochemical and paleontological evidence from three sections in the Great Basin region, western USA, support the notion that anoxia was widespread, albeit spatially and temporally variable on local scales, along the Laurentian margin during the Early Ordovician. Proxies for anoxia are based on parallel $\delta^{13}C_{carb}$ and $\delta^{34}S_{CAS}$ excursions that affected the global carbon and sulfate reservoirs, which occur near the North American Skullrockian–Stairsian Stage boundary. These positive excursions roughly coincide with near zero I/Ca ratios that are more indicative of local water column anoxia or where the oxygen chemocline has impinged upon the seafloor. At Ibex, Utah a 30% decrease in standing diversity occurs during both isotope excursions. The I/Ca proxy is consistent with the hypothesis that base-Stairsian trilobite extinction was caused by anoxia, previously only supported by traditional geochemical proxies for anoxia (positive $\delta^{13}C$ and $\delta^{34}S$ excursions). This base-Stairsian trilobite extinction and geochemical perturbation represents one of the last well-documented recurrent anoxic events that plagued Cambrian–Ordovician shallow marine communities. Biodiversity levels quickly returned to pre-extinction levels by the end of the global anoxic event and continued to rise as part of the Great Ordovician Biodiversification Event.

Acknowledgements

Linda Kah, Jeremy Owens, an anonymous reviewer, and co-editor-in-chief Derek Vance are thanked for their constructive reviews that improved an earlier version of this paper. This paper is a contribution to IGCP Projects 591 and 653. Many thanks to Anthony Love (Appalachian State University) for thin section preparation and Eric Hiatt (University of Wisconsin–Oshkosh) for discussion and technical support using the CL microscope. CTE was supported by the Evolving Earth Foundation, a Geological Society of America Graduate Student Research Grant, and a Paleontological Society Student Research Grant. Funding was also provided in part by NSF Grants EAR-0819832 and EAR-0745452 (MRS), EAR-1349252 and OCE-1232620 (Z. Lu), and the Packard Fellowship in Science and Engineering (DAF).

Appendix A. Supplementary material

Supplementary material related to this article can be found online at https://doi.org/10.1016/j.epsl.2017.10.002.

References

Adams, D.D., Hurtgen, M.T., Sageman, B.B., 2010. Volcanic triggering of a biogeochemical cascade during Oceanic Anoxic Event 2. Nat. Geosci. 3, 201–204. http://dx.doi.org/10.1038/ngeo743.

Adrain, J.M., Westrop, S.R., Karim, T.S., Landing, E., 2014. Trilobite biostratigraphy of the Stairsian Stage (upper Tremadocian) of the Ibexian Series, Lower Ordovician, western United States. Mem. Assoc. Australas. Palaeontol. 45, 167–214.

Bambach, R.K., Knoll, A.H., Wang, S.C., 2004. Origination, extinction, and mass depletions of marine diversity. Paleobiology 30, 522–542.

Berner, R.A., 2006. GEOCARBSULF: a combined model for Phanerozoic atmospheric O_2 and CO_2. Geochim. Cosmochim. Acta 70, 5653–5664. http://dx.doi.org/10.1016/j.gca.2005.11.032.

Berner, R.A., VandenBrooks, J.M., Ward, P.D., 2007. Oxygen and evolution. Science 316, 557–558.

Blakey, R.C., 2011. Middle Ordovician North American Paleogeographic Map.

Brand, U., Veizer, J., 1980. Chemical diagenesis of a multicomponent carbonate system-1: trace elements. J. Sediment. Res. 50, 1219–1236. http://dx.doi.org/10.1306/212F7BB7-2B24-11D7-8648000102C1865D.

Campos, M.L.A.M., Sanders, R., Jickells, T., 1999. The dissolved iodate and iodide distribution in the South Atlantic from the Weddell Sea to Brazil. Mar. Chem. 65, 167–175.

Canfield, D.E., 2001. Biogeochemistry of Sulfur Isotopes. Rev. Mineral. Geochem. 43, 607–636. http://dx.doi.org/10.2138/gsrmg.43.1.607.

Chance, R., Baker, A.R., Carpenter, L., Jickells, T.D., 2014. Environmental science: processes & impacts supplementary files publication details. In: Environ. Sci. Process. Impacts, vol. 16, pp. 1841–1859.

Chance, R., Weston, K., Baker, A.R., Hughes, C., Malin, G., Carpenter, L., Meredith, M.P., Clarke, A., Jickells, T.D., Mann, P., Rossetti, H., 2010. Seasonal and interannual variation of dissolved iodine speciation at a coastal Antarctic site. Mar. Chem. 118, 171–181. http://dx.doi.org/10.1016/j.marchem.2009.11.009.

Cooper, R.A., Sadler, P.M., 2012. The Ordovician Period. In: Gradstein, F.M., Ogg, J.G., Schmitz, M. (Eds.), The Geologic Time Scale 2012. Elsevier Science & Technology, Amsterdam, pp. 489–523.

Edwards, C.T., Saltzman, M.R., 2014. Carbon isotope ($\delta^{13}C_{carb}$) stratigraphy of the Lower–Middle Ordovician (Tremadocian–Darriwilian) in the Great Basin, western United States: implications for global correlation. Palaeogeogr. Palaeoclimatol. Palaeoecol. 399, 1–20.

Edwards, C.T., Saltzman, M.R., 2016. Paired carbon isotopic analysis of Ordovician bulk carbonate ($\delta^{13}C_{carb}$) and organic matter ($\delta^{13}C_{org}$) spanning the Great Ordovician Biodiversification Event. Palaeogeogr. Palaeoclimatol. Palaeoecol. 458, 102–117.

Ethington, R.L., Clark, D.L., 1981. Lower and Middle Ordovician conodonts from the Ibex area, western Millard County, Utah. Brigh. Young Univ. Geol. Stud. 28, 1–155.

Fike, D.A., Grotzinger, J.P., Pratt, L.M., Summons, R.E., 2006. Oxidation of the Ediacaran ocean. Nature 444, 744–747. http://dx.doi.org/10.1038/nature05345.

Gill, B.C., Lyons, T.W., Frank, T.D., 2008. Behavior of carbonate-associated sulfate during meteoric diagenesis and implications for the sulfur isotope paleoproxy. Geochim. Cosmochim. Acta 72, 4699–4711.

Gill, B.C., Lyons, T.W., Saltzman, M.R., 2007. Parallel, high-resolution carbon and sulfur isotope records of the evolving Paleozoic marine sulfur reservoir. Palaeogeogr. Palaeoclimatol. Palaeoecol. 256, 156–173.

Gill, B.C., Lyons, T.W., Young, S.A., Kump, L.R., Knoll, A.H., Saltzman, M.R., 2011. Geochemical evidence for widespread euxinia in the later Cambrian ocean. Nature 469, 80–83.

Gomes, M.L., Hurtgen, M.T., Sageman, B.B., 2016. Biogeochemical sulfur cycling during Cretaceous oceanic anoxic events: a comparison of OAE1a and OAE2. Paleoceanography 31, 233–251. http://dx.doi.org/10.1002/2015PA002869.

Hardisty, D.S., Lu, Z., Planavsky, N.J., Bekker, A., Philippot, P., Zhou, X., Lyons, T.W., 2014. An iodine record of Paleoproterozoic surface ocean oxygenation. Geology 42, 619–622. http://dx.doi.org/10.1130/G35439.1.

Hardisty, D.S., Lu, Z., Bekker, A., Diamond, C.W., Gill, B.C., Jiang, G., Kah, L.C., Knoll, A.H., Loyd, S.J., Osburn, M.R., Planavsky, N.J., Wang, C., Zhou, X., Lyons, T.W., 2017. Perspectives on Proterozoic surface ocean redox from iodine contents in ancient and recent carbonate. Earth Planet. Sci. Lett. 463, 159–170. http://dx.doi.org/10.1016/j.epsl.2017.01.032.

Hiatt, E.E., Pufahl, P.K., 2014. Chapter 5: Cathodoluminescence petrography of carbonate rocks: a review of applications for understanding diagenesis, reservoir quality, and pore system evolution. In: Mineralogical Association of Canada Short Course, vol. 45, pp. 75–96.

Hintze, L.F., 1951. Lower Ordovician detailed stratigraphic sections for western Utah. Bull. Utah Geol. Mineral Surv. 39, 1–99.

Hintze, L.F., 1973. Lower and Middle Ordovician stratigraphic sections in the Ibex area, Millard County, Utah. Brigh. Young Univ. Geol. Stud. 20, 3–36.

Jin, C., Li, C., Algeo, T.J., Planavsky, N.J., Cui, H., Yang, X., Zhao, Y., Zhang, X., Xie, S., 2016. A highly redox-heterogeneous ocean in South China during the early Cambrian (~529–514 Ma): implications for biota-environment co-evolution. Earth Planet. Sci. Lett. 441, 38–51. http://dx.doi.org/10.1016/j.epsl.2016.02.019.

Jones, D.S., Fike, D.A., 2013. Dynamic sulfur and carbon cycling through the end-Ordovician extinction revealed by paired sulfate-pyrite $\delta^{34}S$. Earth Planet. Sci. Lett. 363, 144–155. http://dx.doi.org/10.1016/j.epsl.2012.12.015.

Kah, L.C., Thompson, C.K., Henderson, M.A., Zhan, R., 2016. Behavior of marine sulfur in the Ordovician. Palaeogeogr. Palaeoclimatol. Palaeoecol. 458, 133–153. http://dx.doi.org/10.1016/j.palaeo.2015.12.028.

Leavitt, W.D., Halevy, I., Bradley, A.S., Johnston, D.T., 2013. Influence of sulfate reduction rates on the Phanerozoic sulfur isotope record. Proc. Natl. Acad. Sci. USA 110, 11244–11249. http://dx.doi.org/10.1073/pnas.1218874110.

Li, C., Love, G.D., Lyons, T.W., Fike, D.A., Sessions, A.L., Chu, X., 2010. A stratified redox model for the Ediacaran ocean. Science 328, 80–83. http://dx.doi.org/10.1126/science.1182369.

Lowrie, W., Alvarez, W., 1984. Lower Cretaceous magnetic stratigraphy in Umbrian pelagic limestone sections. Earth Planet. Sci. Lett. 71, 315–328.

Lu, Z., Hoogakker, B.A.A., Hillenbrand, C.-D., Zhou, X., Thomas, E., Gutchess, K.M., Lu, W., Jones, L., Rickaby Rosalind, E.M., 2016. Oxygen depletion recorded in upper waters of the glacial Southern Ocean. Nat. Commun. 7, 1–8. http://dx.doi.org/10.1038/pj.2016.37.

Lu, Z., Jenkyns, H.C., Rickaby, R.E.M., 2010. Iodine to calcium ratios in marine carbonate as a paleo-redox proxy during oceanic anoxic events. Geology 38, 1107–1110. http://dx.doi.org/10.1130/G31145.1.

Marenco, P.J., Corsetti, F.A., Hammond, D.E., Kaufman, A.J., Bottjer, D.J., 2008. Oxidation of pyrite during extraction of carbonate associated sulfate. Chem. Geol. 247, 124–132. http://dx.doi.org/10.1016/j.chemgeo.2007.10.006.

McInerney, F.A., Wing, S.L., 2011. The Paleocene–Eocene Thermal Maximum: a perturbation of carbon cycle, climate, and biosphere with implications for the future. Annu. Rev. Earth Planet. Sci. 39, 489–516.

Miller, J.F., Evans, K.R., Dattilo, B.F., 2012. Chapter 31: The Great American Carbonate Bank in the Miogeocline of Western Central Utah: Tectonic Influences on Sedimentation. In: Gt. Am. Carbonate Bank. In: AAPG Mem., vol. 98, pp. 769–854.

Ostrander, C.M., Owens, J.D., Nielsen, S.G., 2017. Constraining the rate of oceanic deoxygenation leading up to a Cretaceous Oceanic Anoxic Event (OAE-2: ∼94 Ma). Sci. Adv. 3, e1701020.

Owens, J.D., Gill, B.C., Jenkyns, H.C., Bates, S.M., Severmann, S., Kuypers, M.M.M., Woodfine, R.G., Lyons, T.W., 2013. Sulfur isotopes track the global extent and dynamics of euxinia during Cretaceous Oceanic Anoxic Event 2. Proc. Natl. Acad. Sci. USA 110, 18407–18412. http://dx.doi.org/10.1073/pnas.1305304110.

Owens, J.D., Lyons, T.W., Hardisty, D.S., Lowery, C.M., Lu, Z., Lee, B., Jenkyns, H.C., 2017. Patterns of local and global redox variability during the Cenomanian–Turonian Boundary Event (Oceanic Anoxic Event 2) recorded in carbonates and shales from central Italy. Sedimentology 64, 168–185. http://dx.doi.org/10.1111/sed.12352.

Owens, J.D., Reinhard, C.T., Rohrssen, M., Love, G.D., Lyons, T.W., 2016. Empirical links between trace metal cycling and marine microbial ecology during a large perturbation to Earth 's carbon cycle. Earth Planet. Sci. Lett. 449, 407–417. http://dx.doi.org/10.1016/j.epsl.2016.05.046.

Reinhard, C.T., Planavsky, N.J., Robbins, L.J., Partin, C.A., Gill, B.C., Lalonde, S.V., Bekker, A., Konhauser, K.O., Lyons, T.W., 2013. Proterozoic ocean redox and biogeochemical stasis. Proc. Nat. Acad. Sci. USA 110, 5357–5362. http://dx.doi.org/10.1073/pnas.1208622110.

Ross, R.J.J., 1964. Middle and lower Ordovician formations in southernmost Nevada and adjacent California. United States Geol. Surv. Bull. 1180–C, 1–101.

Ross, R.J.J., James, N.P., Hintze, L.F., Poole, F.G., 1989. Architecture and evolution of a Whiterockian (early middle Ordovician) carbonate platform, basin ranges of western U.S.A. In: Control. Carbonate Platf. Basin Dev., pp. 167–186.

Rue, E.L., Smith, G.J., Cutter, G.A., Bruland, K.W., 1997. The response of trace element redox couples to suboxic conditions in the water column. Deep. Res. 44, 113–134.

Saltzman, M.R., Edwards, C.T., Adrain, J.M., Westrop, S.R., 2015. Persistent oceanic anoxia and elevated extinction rates separate the Cambrian and Ordovician radiations. Geology 43, 807–810. http://dx.doi.org/10.1130/G36814.1.

Saltzman, M.R., Young, S.A., Kump, L.R., Gill, B.C., Lyons, T.W., Runnegar, B., 2011. Pulse of atmospheric oxygen during the late Cambrian. Proc. Natl. Acad. Sci. USA 108, 3876–3881. http://dx.doi.org/10.1073/pnas.1011836108.

Sim, M.S., Ono, S., Donovan, K., Templer, S.P., Bosak, T., 2011. Effect of electron donors on the fractionation of sulfur isotopes by a marine Desulfovibrio sp. Geochim. Cosmochim. Acta 75, 4244–4259. http://dx.doi.org/10.1016/j.gca.2011.05.021.

Sweet, W.C., Tolbert, C.M., 1997. An Ibexian (Lower Ordovician) reference section in the Southern Egan Range, Nevada, for a conodont-based chronostratigraphy. In: Taylor, M.E. (Ed.), Early Paleozoic Biochronology of the Great Basin, Western United States. In: U.S. Geological Survey Professional Paper, vol. 1579. U.S. Geological Survey, Washington, pp. 53–88.

Trotter, J.A., Williams, I.S., Barnes, C.R., Lécuyer, C., Nicoll, R.S., 2008. Did cooling oceans trigger Ordovician biodiversification? Evidence from conodont thermometry. Science 321, 550–554. http://dx.doi.org/10.1126/science.1155814.

Tucker, M.E., Wright, V.P., 1990. Carbonate Sedimentology. Blackwell-Science Ltd., Oxford.

Wotte, T., Shields-Zhou, G.A., Strauss, H., 2012. Carbonate-associated sulfate: experimental comparisons of common extraction methods and recommendations toward a standard analytical protocol. Chem. Geol. 326–327, 132–144. http://dx.doi.org/10.1016/j.chemgeo.2012.07.020.

Zhou, X., Jenkyns, H.C., Lu, W., Hardisty, D.S., Owens, J.D., Lyons, T.W., Lu, Z., 2017. Organically bound iodine as a bottom-water redox proxy: preliminary validation and application. Chem. Geol. 457, 95–106. http://dx.doi.org/10.1016/j.chemgeo.2017.03.016.

Zhou, X., Jenkyns, H.C., Owens, J.D., Junium, C.K., Zheng, X.Y., Sageman, B.B., Hardisty, D.S., Lyons, T.W., Ridgwell, A., Lu, Z., 2015. Upper ocean oxygenation dynamics from I/Ca ratios during the Cenomanian–Turonian OAE 2. Paleoceanography 30, 510–526. http://dx.doi.org/10.1002/2014PA002741.

Zhou, X., Thomas, E., Rickaby Rosalind, E.M., Winguth, A.M.E., Lu, Z., 2014. I/Ca evidence for upper ocean deoxygenation during the PETM. Paleoceanography 29, 964–975. http://dx.doi.org/10.1002/2014PA002702.Received.

Zhou, X., Thomas, E., Winguth, A.M.E., Ridgwell, A., Scher, H., Hoogakker, B.A.A., Rickaby, R.E.M., Lu, Z., 2016. Expanded oxygen minimum zones during the late Paleocene–early Eocene: hints from multiproxy comparison and ocean modeling. Paleoceanography 31, 1532–1546. http://dx.doi.org/10.1002/2016PA003020.